Computing and Informatics, Vol. 44, 2025, 882–914, doi: 10.31577/cai_2025_4_882

FAULT FEATURE EXTRACTION IN ROLLING BEARINGS USING TIME-FREQUENCY ANALYSIS AND OPTIMIZED VARIATIONAL MODE DECOMPOSITION

Xuezhen Cheng, Chuannuo Xu, Hanlin Sun, Jiming Li*

College of Electrical Engineering and Automation
Shandong University of Science and Technology
No. 579, Qianwangang Road, Huangdao District
Qingdao, China
e-mail: skd993996@sdust.edu.cn

Abstract. This paper focuses on the analysis of rolling bearing vibration signal, presenting a comprehensive investigation into vibration signal analysis and fault signal feature extraction methods. The research primarily investigates a Variational Modal Decomposition (VMD) method, with enhancements made through the Tucked Swarm Algorithm (TSA) optimization and the use of Maximum Correlated Kurtosis Deconvolution (MCKD). It proposes a method for identifying the optimal parameter configurations for VMD. The proposed method is applied to analyze the rolling bearing vibration signal, and its efficacy in feature extraction has been validated through comparative analysis. This study employs a feature extraction methodology using kurtosis, envelope spectral kurtosis, and other indicators as basic features of vibration signals. It constructs a multi-feature feature vector dataset and utilizes the Least Squares Support Vector Machine (LSSVM) as a fault type classifier to validate the effectiveness of the proposed feature extraction method. The results demonstrate that the fault identification accuracy achieved by the proposed method consistently exceeds 96 %.

Keywords: Rolling bearings, feature extraction, variational mode decomposition, tucked swarm algorithm, maximum correlation kurtosis deconvolution

* Corresponding author

1 INTRODUCTION

Rolling bearings constitute pivotal elements in rotating mechanical equipment. Throughout their operational lifespan, they frequently encounter issues such as fatigue peeling [1], fractures [2], wear [3], corrosion [4], and other failures, stemming from prolonged continuous operation and challenging industrial environments. These failures significantly impede the secure operation of mechanical equipment. Consequently, monitoring the operational status of bearings and promptly detecting bearing faults that emerge are critical measures to ensure industrial safety in production. Currently, vibration signals serve as a common tool for diagnosing bearing faults. However, despite the extensive use of Empirical Mode Decomposition (EMD) [5, 6] to tackle the significant challenges posed by the nonlinear and non-stationary characteristics and strong environmental noise in extracting fault features from vibration signals, this method is susceptible to mode aliasing and end effects during the signal decomposition process. Other EMD techniques, such as Ensemble Empirical Mode Decomposition (EEMD) [7, 8], Complementary Ensemble Empirical Mode Decomposition (CEEMD) [9], and Complementary Ensemble Empirical Mode Decomposition with Adaptive Noise (CEEMDAN) [10], introduce white noise to the original signal and subsequently average the Intrinsic Mode Functions (IMFs) to alleviate the impact of modal aliasing and end effects. Despite the improvement in signal processing performance offered by EMD-like methods, they do not entirely eliminate these inherent drawbacks. To effectively address this issue, Dragomiretskiy et al. [11] introduce VMD, a method that decomposes signals into a predetermined number of modes, each possessing a limited bandwidth. The imposition of bandwidth limitations is pivotal for mitigating mode aliasing and end effects. Consequently, the selection of the decomposition mode number K and the quadratic penalty factor for VMD becomes crucial.

To determine the optimal number of decomposition modes K and the quadratic penalty factor value, researchers have utilized various optimization algorithms, such as genetic algorithms [12, 13], particle swarm optimization [14, 15], and grey wolf algorithms [16]. Despite these improvements, extracting comprehensive fault information from Intrinsic Mode Function (IMF) components alone remains a challenge. This difficulty is compounded by the inherent limitations of the algorithms, including their tendency to get trapped in local optima and the difficulties they face in achieving convergence.

In light of these challenges, this paper introduces a VMD-based multi-feature extraction approach for fault analysis. This approach leverages the combined optimization of the Tucked Swarm Algorithm (TSA) [17] and Maximum Correlated Kurtosis Deconvolution (MCKD) [18] to enhance the feature extraction process. The approach first uses correlation kurtosis as the fitness function for TSA optimization, followed by the application of MCKD to the IMF components. This process aims to reduce environmental noise and accentuate periodic fault pulses, ultimately determining the optimal values for the decomposition mode number K and quadratic penalty factor for VMD. To enhance the accuracy of fault information extraction,

this paper constructs a multi-feature vector dataset for bearing faults, incorporating seven indicators such as envelope entropy [19], kurtosis, and related derivative indicators [20, 21]. Subsequently, utilizing this dataset, the least squares support vector machine is employed for fault identification. The results demonstrate that the recognition rate of the feature vectors extracted by this method surpasses 96 %, representing a significant improvement over other VMD optimization approaches.

The contributions of this paper are summarized as follows:

1. A Variational Modal Decomposition (VMD) method based on Tucked Swarm Algorithm (TSA) and Maximum Correlated Kurtosis Deconvolution (MCKD) is proposed to obtain the optimal combination of K and α parameters in VMD.

2. Using kurtosis, envelope spectrum kurtosis and other indexes as the feature extraction method for the basic features of vibration signals, a multi-feature-based feature vector data set is constructed, and the Least Squares Support Vector Machine (LSSVM) is used as the fault type classifier to verify the effectiveness of the feature extraction method proposed in this paper.

The remainder of the paper is organized into five sections. In Section 2 we introduce an improved VMD parameter optimization method. In Section 3 we investigate fault feature extraction methods for rolling bearings. Section 4 is dedicated to the experimental design. Section 5 covers the experimental verification. Section 6 concludes the paper.

2 ON IMPROVED VMD PARAMETER OPTIMIZATION METHOD

2.1 VMD Parameter Setting Method

The VMD method involves setting several parameters, namely the decomposition mode number K, quadratic penalty factor α, noise tolerance τ, and recognition accuracy ε. Compared with the first two parameters, noise tolerance τ, and recognition accuracy ε have a relatively minor impact on the decomposition performance of the VMD method. Typically, based on empirical knowledge, these latter parameters are set to default values. The primary focus of this section is to investigate the numerical configurations of the decomposition mode number K and the quadratic penalty factor α in the VMD method. Additionally, the section aims to optimize the VMD through the TSA algorithm to identify the optimal parameter combination of K and α.

Before the tucked performs jet propulsion, in order to avoid conflicts caused by repeated individual positions, new individual positions need to be calculated for the

randomly distributed tucked swarm, and the following equations are met:

$$\begin{aligned} \vec{N} &= \frac{\vec{G}}{\vec{M}}, \\ \vec{G} &= c_2 + c_3 - \vec{F}, \\ \vec{F} &= 2c_1, \\ \vec{M} &= \left| P_{min} + c_1 \cdot P_{max} - P_{min} \right|, \end{aligned} \tag{1}$$

where $\vec{G}$ is the gravity of the individual; $\vec{F}$ is the advection force of deep-sea current; $\vec{M}$ is the social force between individuals; c_1, c_2, and c_3 are the three random values in the value range of $[0, 1]$. P_{min} and P_{max} represent the initial speed and auxiliary speed of communication between individuals respectively, and their values are generally set between $[1, 4]$.

After avoiding the conflict in the foraging process, the population will move closer to the optimal neighbor position. The formula for the distance between the individual and the food in the x iteration is defined as follows:

$$\vec{PD} = \left| \vec{FS} - r_{and} \cdot \vec{P_P}(x) \right|, \tag{2}$$

where $\vec{P_P}(x)$ represents individual position; $\vec{FS}$ indicates the location of food; x represents the number of iterations of the method; r_{and} is the random number between [0, 1]; $\vec{PD}$ indicates the distance between the individual's position and the food's position.

The size of the random value r_{and} determines the way in which the tucked individual approaches the position of the optimal seeking individual, as shown in Equation (3):

$$\vec{P_P}(x') = \begin{cases} \vec{FS} + \vec{N} \cdot \vec{PD}, & r_{and} \geq or \geq 0.5, \\ \vec{FS} - \vec{N} \cdot \vec{PD}, & r_{and} < 0.5, \end{cases} \tag{3}$$

where $\vec{P_P}(x')$ indicates the position of individual update.

In order to better simulate the group behavior of the tucked swarm, the first two optimal solutions obtained in the iterative optimization process are retained to obtain the position of the tucked individual, and according to this, the position of other encapsulated individuals is updated. Its behavior is described as Equation (4):

$$\vec{P_P}(x+1) = \frac{\vec{P_P}(x) + \vec{P_P}(x+1)}{2 + c_1}. \tag{4}$$

Tucked Swarm Algorithm flow:

1. The tucked swarm $\vec{P_P}$ is initialized, the initial location of the tucked swarm $\vec{P_P}(x_i)$ is randomly generated, and the boundary parameters of the population are defined;

2. The fitness value of each tucked individual was calculated according to the location of the tucked individual, and the optimal value of the current fitness and the corresponding individual location were recorded;
3. Update the position of each individual in the population according to the group behavior of the population, and adjust the position of the individual beyond the given search range boundary;
4. Calculate the fitness value of the tucked individual after updating the location. If the current fitness is better than the previous fitness, the current fitness will be updated to the optimal value, and the corresponding optimal position will also be updated;
5. Determine whether iteration can be stopped. If yes, the iteration stops and the optimal value of the current fitness is output. If not, repeat steps 3 to 5.

The flow of the tucked swarm algorithm is shown in Figure 1.

The data used in this paper are from the rolling bearing public data set of Case Western Reserve University. It is mainly composed of power tester, encoder and three-phase motor. The bearing under test supports the rotating shaft of the motor, and the sampling frequency of the driving end bearing is 12 KHz and 48 KHz, and the sampling frequency of the fan end bearing is 12 KHz. The vibration sensor is used to collect the original data at the motor drive end (DE) and fan end (FE), and the obtained data files are stored in the .mat file format of MATLAB software. In actual working conditions, the vibration signals of rolling bearings with the same type of fault are very close to each other under different damage sizes, so only one vibration signal can be selected for analysis and re-search. The vibration signal selected in this paper is the fault signal of the outer ring, inner ring and rolling element of the rolling bearing with speed of 1772 rpm, damage size of 0.1778 mm and load of 1 HP. The details are shown in Table 1.

Types of rolling bearing faults	Speed [rpm]	Fault diameter [mm]	Load [HP]
Inner ring failure	1 772	0.1778	1
Outer ring malfunction	1 772	0.1778	1
Rolling element failure	1 772	0.1778	1

Table 1. Fault size information for rolling bearings

Utilizing the outer ring fault signals from the publicly available rolling bearings dataset at Case Western Reserve University as a case study, this study explores the numerical selection of decomposition mode numbers. Drawing from empirical knowledge, the secondary penalty factor was set to 2 000, and the decomposition mode numbers are individually configured as 3, 4, 5, and 6. Subsequently, VMD decomposition is executed on the outer ring fault signal, and the outcomes are visually represented in Figure 2. The central frequencies of each IMF component for the outer ring fault signal under the four aforementioned parameter combinations are presented in Table 2.

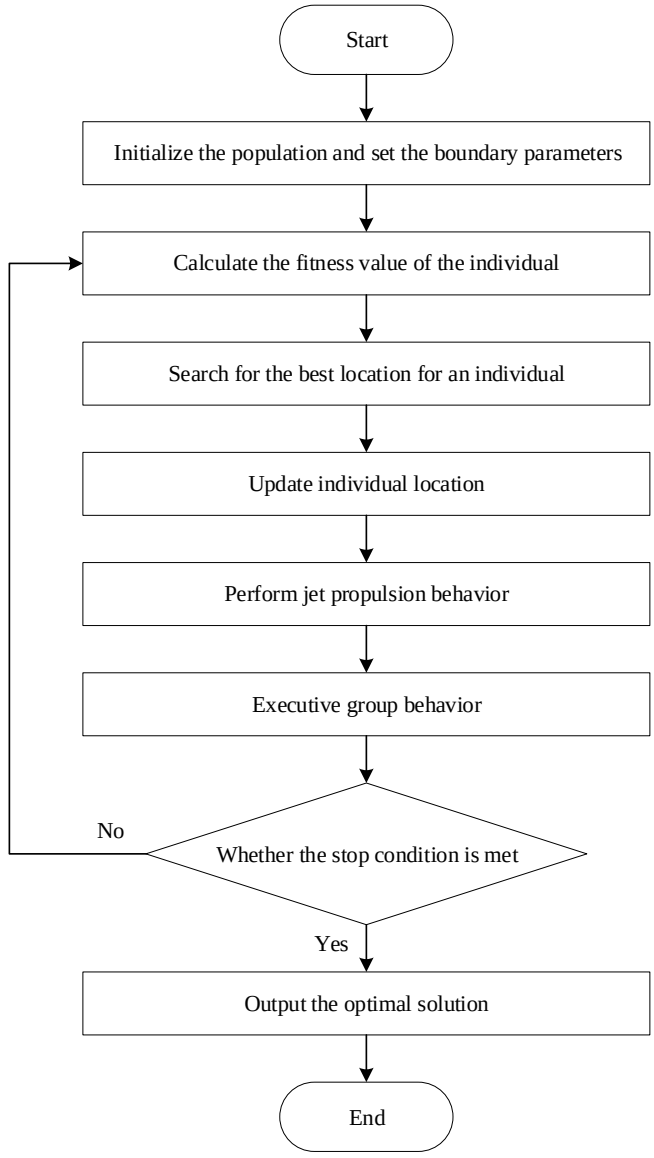

Figure 1. Flow chart of tucked swarm algorithm

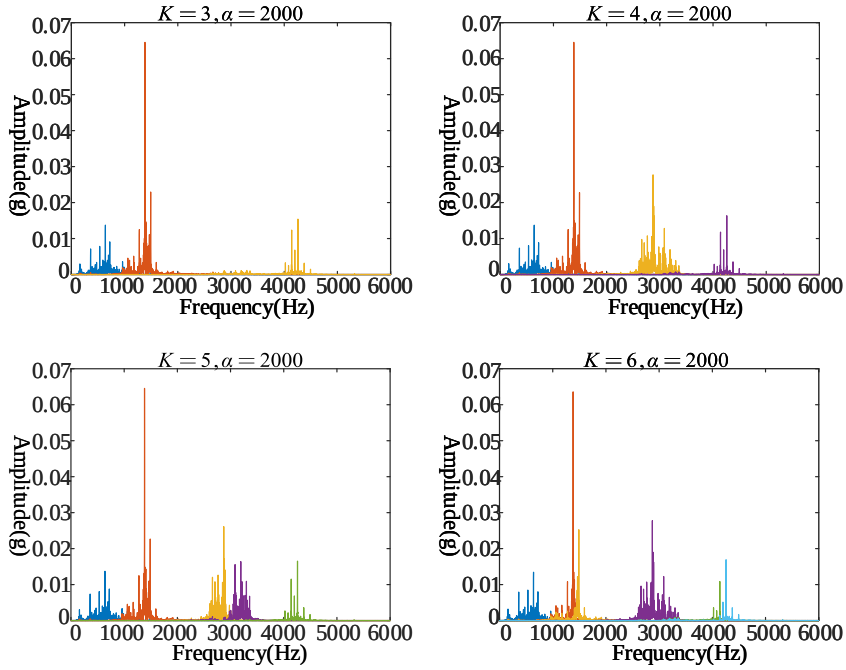

Figure 2. Spectral graph of VMD decomposition

Decomposition Mode Number K	C_{12}	C_{23}	C_{34}	C_{45}	C_{56}
3	0.0092	0.0412	–	–	–
4	0.0032	0.0040	0.0030	–	–
5	0.0027	0.0031	0.0022	0.0972	–
6	0.0012	0.0009	0.0013	0.0070	0.0139

Table 2. Adjacent IMF correlation coefficients corresponding to different K values

Based on the observations in Figure 2 and Table 2, it is evident that setting the quadratic penalty factor α to 2000 progressively reduces the bandwidth of each IMF component as the number of decomposed modes K increases. According to the central frequency observation method, the appropriate value for K can be determined.

As indicated in Table 2, when $K = 3$, the signal cannot be fully decomposed, resulting in under-decomposition. When $K = 5$, a substantial overlap occurs between the center frequencies of IMF3 (1286.6 Hz) and IMF4 (1304.5 Hz), potentially causing mode aliasing and leading to over-decomposition. Conversely, when $K = 4$, the center frequencies of each IMF component exist independently, demonstrating no noticeable mode mixing phenomenon. Currently, the central frequency observation

method lacks a clear theoretical basis for assessing mode mixing, over-decomposition, and under-decomposition in IMF components.

Additionally, there is a degree of subjectivity in determining whether the central frequency values of the IMF components are sufficiently close to each other. To further elucidate the selection of the decomposition mode number K, this paper analyzes the correlation coefficients of adjacent IMF components under different decomposition mode numbers. Table 3 reveals that when the decomposition mode number K is less than 5, the correlation coefficient values of adjacent IMF components are all below 0.01, indicating normal signal decomposition. However, when K equals 5, the correlation coefficients between IMF4 and IMF5 experience a sudden change, signifying the occurrence of mode aliasing and resulting in signal over-decomposition. Consequently, in studying the impact of different α values on signal decomposition, it is advisable to set K to 4.

Decomposition Mode Number K	Center Frequency [Hz]						
3	195.4	1 203.6	1 882.6	–	–	–	–
4	186.7	445.1	1 299.3	1 882.6	–	–	–
5	186.4	444.9	1 286.6	1 304.5	1 886.6	–	–
6	186.3	444.8	1 190	1 297.9	1 394	1 888	–

Table 3. IMF center frequencies corresponding to different K values

Subsequently, we will discuss the influence of the quadratic penalty factor α on the signal decomposition effect. To illustrate this impact, we take the fault signal from the outer ring of a rolling bearing as an example, focusing on the numerical determination of the quadratic penalty factor α. With a fixed decomposition mode number K of 4, various values of α is employed to scrutinize their effects on signal decomposition. Specifically, α is set to 1 000, 2 000, 4 000, 6 000, 8 000, and 10 000, and each of these parameter combinations will be utilized for VMD decomposition of the outer ring fault signal. The results are displayed in Figure 5. From Figure 4, it is apparent that when $\alpha < 2\,000$, some IMF components may contain frequency components from other sources. On the other hand, when $\alpha > 4\,000$, information is lost due to the gradual reduction of the bandwidth.

Drawing insights from Figure 3, it can be inferred that the optimal value for α lies between 2 000 and 4 000, and the specific value selection entails a certain degree of subjectivity. Besides, employing a fixed method to determine the parameter combination of the decomposition mode number K and the quadratic penalty factor α has inherent limitations, as it neglects the mutual influence between K and α. Consequently, to achieve the optimum decomposition result for Variational Mode Decomposition (VMD), it becomes imperative to refine and optimize the selection method for both the decomposition mode number K and the quadratic penalty factor α.

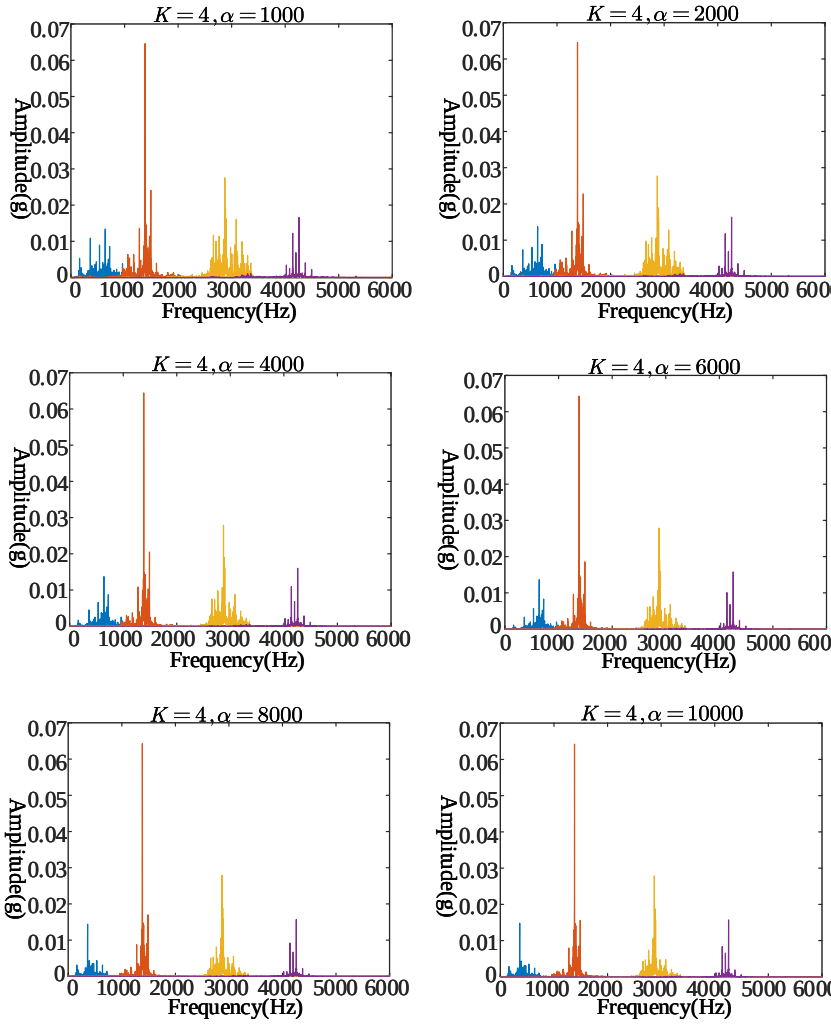

Figure 3. Frequency spectrum charts for different α decompositions with $K = 4$

2.2 VMD Parameter Optimization Method

The selection of a fitness function is a prerequisite for utilizing various intelligent optimization algorithms. Correlation kurtosis, which is based on the concept of kurtosis, incorporates the characteristics of both kurtosis and the correlation coefficient. This enables it to reflect the intensity of specific periodic pulses within a signal. A higher correlation kurtosis value indicates the inclusion of more features related to fault impact information, making the fault features more pronounced.

Conversely, a lower value suggests less evident fault characteristics. Therefore, this paper adopts correlation kurtosis as the fitness function for various intelligent optimization algorithms. Its expression is:

$$CK_M(T) = \frac{\sum_{n=1}^{N}\left(\prod_{m=0}^{M} y_n - mT\right)}{(\sum_{n=1}^{N} y_n^2)^{M+1}}, \tag{5}$$

where y_n represents the vibration signal; T denotes the deconvolution period, signifying the number of data points between two adjacent impulse pulses in the signal; M is the shift number, impacting the quantity of extracted impulse pulses following signal deconvolution.

The fundamental principle of the Variational Mode Decomposition (VMD) method based on Tucked Swarm Algorithm (TSA) and Maximum Correlation Kurtosis Deconvolution (MCKD) optimization (TSA-MCKD-VMD) involves using the correlation kurtosis of each Intrinsic Mode Function (IMF) component obtained through VMD decomposition as the fitness function. The method iteratively searches for the optimal parameter combination for the decomposition mode number K and the quadratic penalty factor α. The specific process of this method is as follows:

1. Initialize the population size N, set the boundary of the positional parameter $Positions[1]$, $Positions[2]$ and the maximum number of iterations $Max_{iteration}$.
2. Calculate the fitness value fitness for each individual with the fitness function.
3. Record the optimal fitness value of the current individual along with its corresponding position, and assess whether the position is optimal.
4. If the current fitness value is optimal, output the current K and α as the optimal parameter combination. In the case where the current fitness value is suboptimal, proceed to update $Positions[1], Positions[2]$ and adjust the search space accordingly.
5. If the method reaches the maximum number of iterations, stop the iteration; Otherwise, proceed to step 2 and continue with the iteration.

   The calculation process of individual fitness value fitness in step 2 is as follows:

   (a) Set the VMD secondary penalty factor $\alpha = Position[1]$, decomposition mode number $K = Positions[2]$, noise tolerance $\tau = 0$, DC component $DC = 0$, and initialize center frequency $int = 1$, with a convergence tolerance $tol =$ 1e−7.
   (b) Perform VMD decomposition to obtain K IMF components.
   (c) Perform MCKD method on K IMF components and set the filter length to 400.
   (d) Obtain the correlation kurtosis $CK_M(T)$ of K IMF components.
   (e) Calculate individual fitness values with formula $fitness = -\sum\{[\max(ck_{iter})]^2\}$.

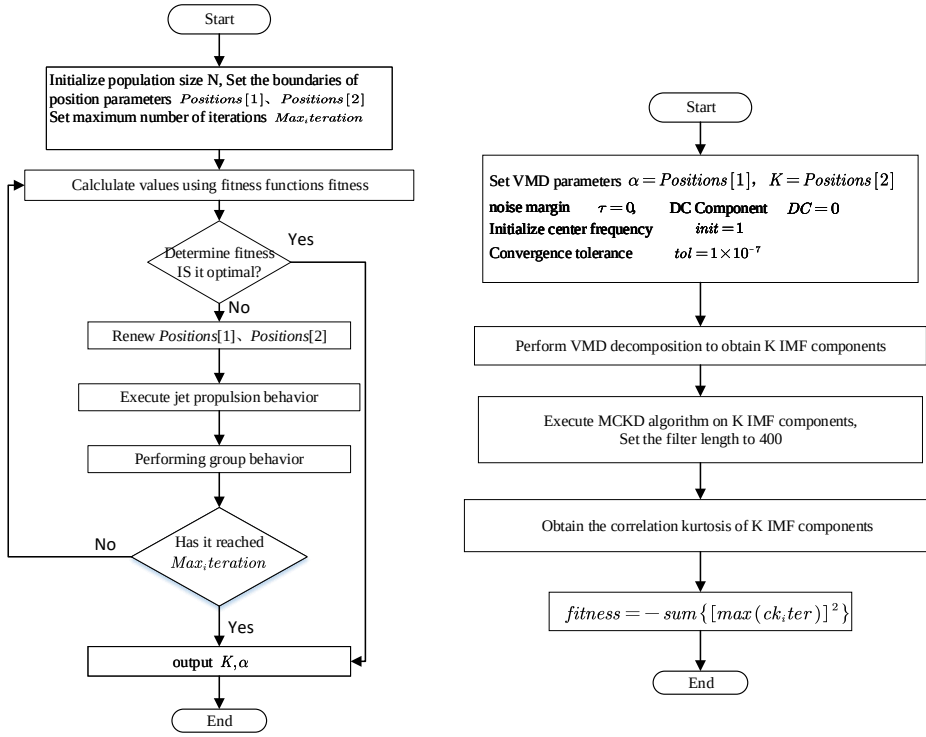

Figure 4. TSA-MCKD-VMD method flowchart

The TSA-MCKD-VMD method flow is shown in Figure 4. The pseudo-code for the algorithm is shown in Algorithm 1.

To prove the superiority of MCKD in accentuating periodic pulse signals associated with faults, this paper takes the simulated signal presented in Figure 5 as an example and makes a comparison between the experimental outcomes of the IMF components obtained through decomposition without MCKD and those obtained with MCKD. The results of these experiments are depicted in Figures 6, 7 and 8.

Through a comparative analysis of experimental results in two distinct scenarios, it becomes evident that MCKD substantially diminishes the noise component within the fault signal. This reduction effectively emphasizes the periodic pulse impact component in the fault signal, thereby enhancing the accuracy of feature extraction for rolling bearing vibration signals.

Algorithm 1 TSA-MCKD-VMD Optimization Algorithm

Input: Vibration signal $x(t)$, population size N, boundaries of parameters T and α, maximum iterations T_{max}
Output: Optimal parameter combination (T_{opt}, α_{opt})
Step 1: Initialization
Initialize population size N, boundaries of parameters T, α, and set T_{max}
Randomly initialize positions of individuals within the boundaries
Step 2: Fitness Calculation
for each individual **do**
    Perform the following steps to calculate the fitness value:
    1. Set VMD parameters:

- Secondary penalty factor α
- Decomposition mode number K
- Noise tolerance, DC component, and initialize center frequency
- Convergence tolerance

    2. Perform VMD decomposition to obtain K IMF components:

$$x(t) = \sum_{k=1}^{K} u_k(t)$$

    where $u_k(t)$ is the k^{th} Intrinsic Mode Function (IMF).
    3. Apply MCKD to each IMF component $u_k(t)$ with a filter length of 400.
    4. Calculate the correlation kurtosis γ_k for each IMF component:

$$\gamma_k = \frac{\mathrm{E}\left[(u_k(t) - \mu_k)^4\right]}{\left(\mathrm{E}\left[(u_k(t) - \mu_k)^2\right]\right)^2}$$

    where μ_k is the mean of $u_k(t)$.
    5. Compute the fitness value for the individual:

$$f(x) = \max_k \gamma_k$$

end for
Step 3: Optimal Evaluation
for each individual **do**
    Record the current fitness value $f(x)$ and corresponding position (T, α)
    if current $f(x)$ is optimal **then**
        Update the best position (T_{opt}, α_{opt})
    else
        Update position and adjust the search space
    end if
end for
Step 4: Iterative Search
for $t = 1$ to T_{max} **do**
    if convergence is reached **then**
        Break the iteration
    else
        Recalculate fitness values and update positions
    end if
end for
Step 5: Output Results
Return (T_{opt}, α_{opt}) as the optimal parameter combination

3 RESEARCH ON FAULT FEATURE EXTRACTION METHODS FOR ROLLING BEARINGS

Feature extraction is a pivotal component of fault diagnosis technology. Kurtosis stands out as one of the most frequently employed feature vectors for discerning

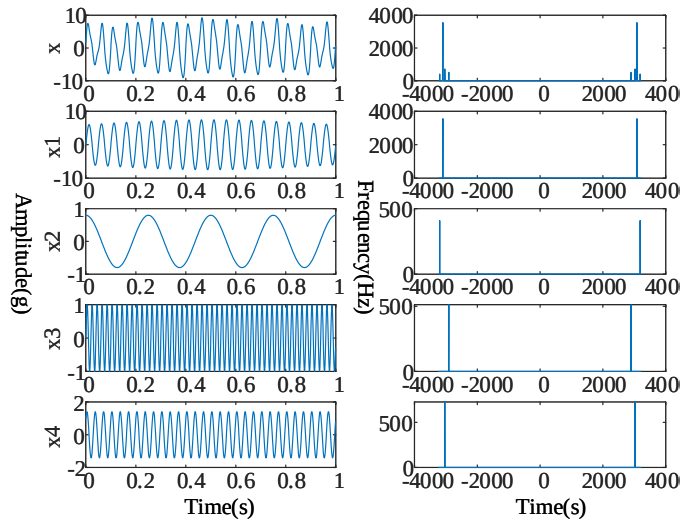

Figure 5. Simulation signal time-domain waveform and frequency-domain diagram

the pulsatility of vibration signals in the time domain. Meanwhile, the envelope spectrum and squared envelope spectrum are extensively utilized to describe the cyclostationarity of vibration signals in the frequency domain. Considering the merits inherent in both kurtosis and envelope-based approaches, hybrid feature vectors, such as envelope spectral kurtosis and set kurtosis, are proposed. To precisely cap-

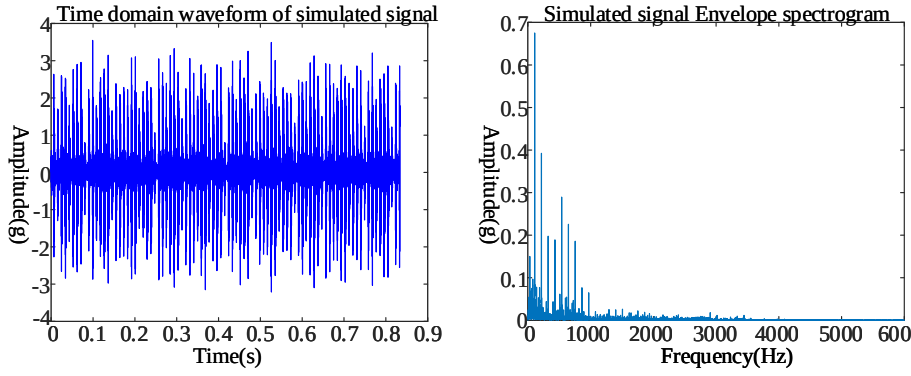

Figure 6. Time domain waveform and envelope spectrum of simulated signals

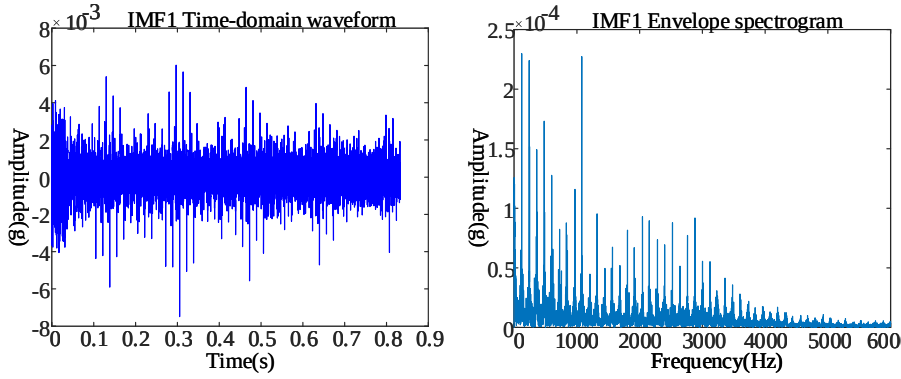

a) IMF1 time-domain waveform and envelope spectrum

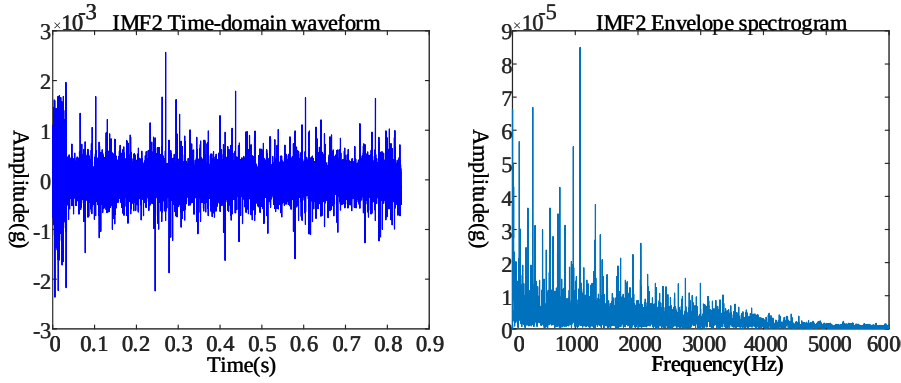

b) IMF2 time-domain waveform and envelope spectrum

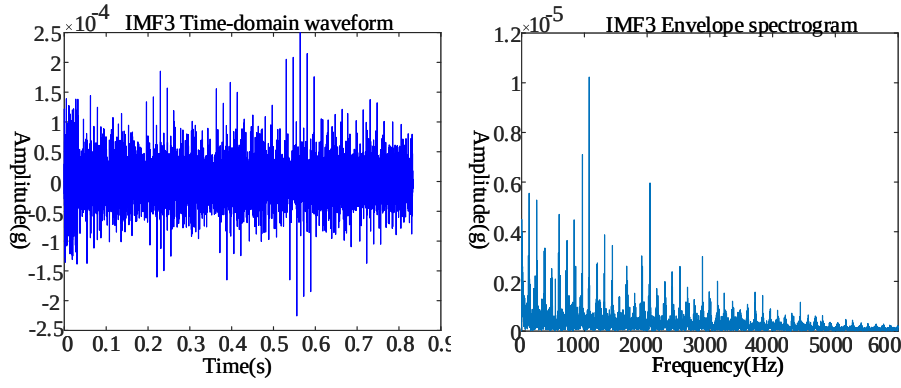

c) IMF3 time-domain waveform and envelope spectrum

Figure 7. Experimental effect without adding MCKD

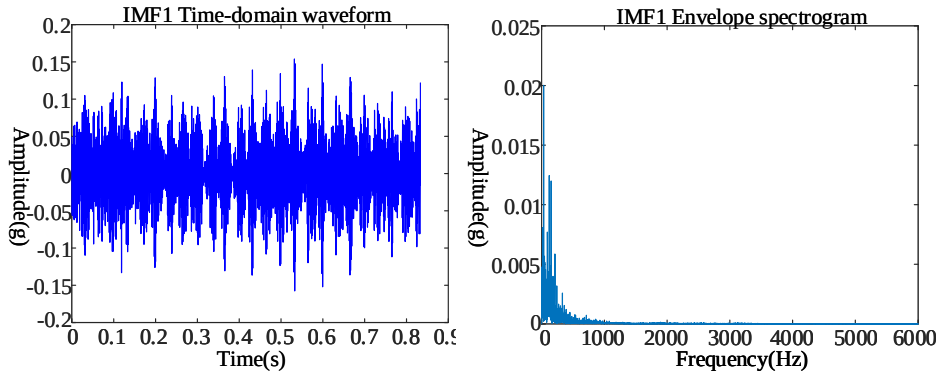

a) IMF1 time-domain waveform and envelope spectrum

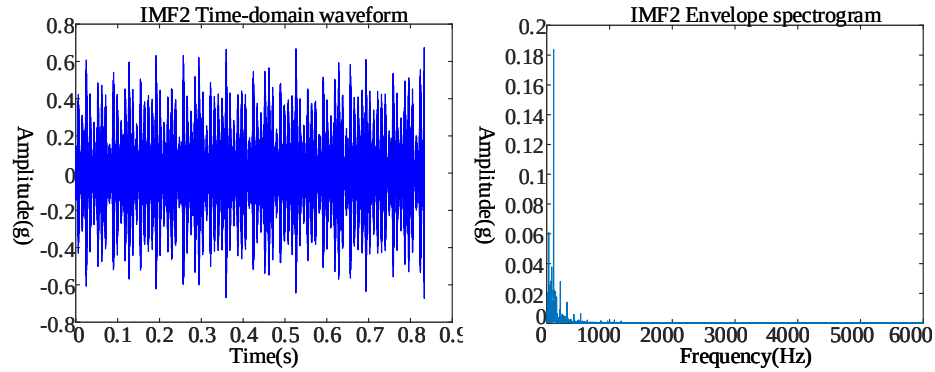

b) IMF2 time-domain waveform and envelope spectrum

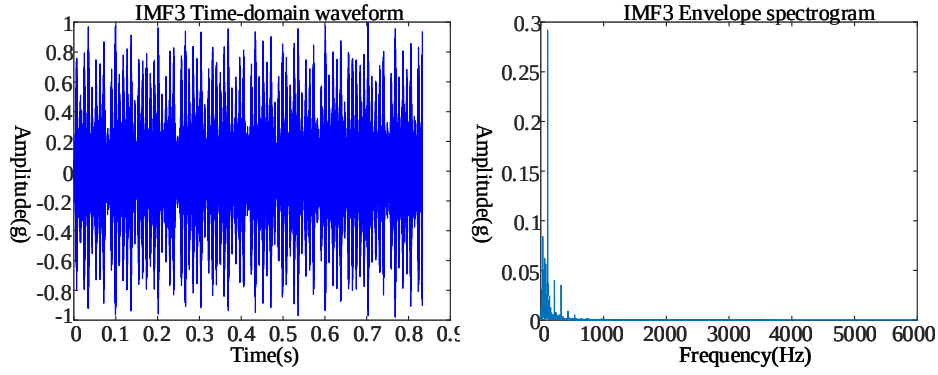

c) IMF3 time-domain waveform and envelope spectrum

Figure 8. Experimental effect of adding MCKD

ture the fault features of complex signals amidst a milieu of intricate noise signals, two novel feature vectors are presented.

Kurtosis is a measure of the non Gaussian nature of random signals, with its formulation expressed as:

$$Kur = \frac{\frac{1}{N}\sum_{i=1}^{N}(x_i - \overline{x})^4}{\left(\frac{1}{N}\sum_{i=1}^{N}(x_i - \overline{x})^2\right)^2}, \tag{6}$$

where x_i is a discrete signal; $\overline{x}$ is the mean of the discrete signal; N is the sampling length.

The kurtosis of the envelope spectrum serves as an effective metric for quantifying and assessing the cyclic stability of the system and has found widespread application in fault identification. The expression for the kurtosis of the signal envelope is:

$$KE = \frac{E\left[E_x - \mu_E\right]^4}{\sigma_E^4}, \tag{7}$$

where E_x is the signal obtained by demodulating the original signal through Hilbert; μ_E is the average value of E_x; σ_E is the standard deviation of E_x; $E[\cdot]$ is the mathematical expectation.

The expression of envelope spectrum kurtosis is:

$$KES = \frac{E\left[ES_x - \mu_{ES}\right]^4}{\sigma_{ES}^4}, \tag{8}$$

where $ES_x = DFT[E_x]$ and DFT are discrete Fourier transforms; μ_{ES} is the average value of ES_x; σ_{ES} is the standard deviation of ES_x; $E[\cdot]$ is the mathematical expectation.

Set kurtosis is a new parameter constructed by kurtosis and envelope spectral kurtosis, with its formulation expressed as:

$$EK = KES{\cdot}Kur. \tag{9}$$

When extracting features from rolling bearings, a single indicator can be easily influenced by complex noise signals, consequently impacting the diagnostic effectiveness. To address this issue, a composite parameter known as weighted kurtosis is proposed, and its expression is:

$$WK = Kur{\cdot}\left|CC\right|, \tag{10}$$

where Kur represents kurtosis; $|CC|$ is the absolute value of the correlation coefficient.

For the real signal $f(n)$, its analytical signal $f_A(n)$ and envelope signal $f_E(n)$

can be obtained:

$$\begin{aligned} f_A(n) &= f(n) + j{\cdot}Hilbert f(n), \\ f_E(n) &= \sqrt{f_{A,re}^2(n) + f_{A,im}^2(n)}, \end{aligned} \tag{11}$$

where j is the imaginary unit; the subscript re and im are the real and imaginary parts, respectively.

The envelope power spectrum of the signal sequence $f(n)$ is calculated:

$$\hat{S_E}(k) = \frac{1}{N}|DFT[f_E(n)]|^2, \tag{12}$$

where $k = 0, 1, \ldots, N-1$; DFT is the discrete Fourier transformation of sample N:

$$DFT[f_E(n)] = \sum_{n=0}^{N-1} f_E(n) e^{-j2\pi kn/N}. \tag{13}$$

The kurtosis of Envelope Power Spectrum (KEPS) is calculated as the ratio of the square of the fourth center moment m_4 to the square of the second center moment m_2:

$$KEPS = \frac{m_4\{\hat{S_E}(k)\}}{(m_2\{\hat{S_E}(k)\})^2}. \tag{14}$$

Due to the increased sparsity of pulse fault features in the envelope power spectrum compared to the traditional envelope spectrum, the parameter $KEPS$ exhibits a heightened capability in detecting fault pulses compared to its counterpart in the traditional envelope spectrum. Furthermore, the correlation coefficient (CC) facilitates the measurement of similarity between the original signal and its decomposition, defined as follows:

$$CC = \frac{E[(u_k - \overline{u_k})(f - \overline{f})]}{E[(u_k - \overline{u_k})^2]E[(f - \overline{f})^2]}, \tag{15}$$

where CC is the correlation coefficient between f and u_k; f and u_k are the original signal and decomposed signal, respectively; $E[\cdot]$ represents mathematical expectation; the $\overline{\ }$ symbol represents the mean.

The expression for SII can be written as:

$$SII = KEPS{\cdot}\left|CC\right|. \tag{16}$$

By leveraging the benefits of envelope power spectrum kurtosis and the correlation coefficient, this method can effectively detect pulse fault information and filter out interfering noise.

For the real signal $f(n)$, the result after $Hilbert$ transformation is as follows:

$$f_H(n) = Hilbert\{f(n)\}. \tag{17}$$

Perform discrete $f_H(n)$ transformation on signal Fourier to obtain the power spectrum $S_H(K)$ of the signal:

$$\begin{aligned} DFT\left|f_H(n)\right| &= \sum_{n=0}^{N-1} f_H(n) e^{-j2\pi kn/N}, \\ S_H(K) &= \frac{1}{N}\left|DFT\left|f_H(n)\right|\right|^2 \quad k = 0, 1, \ldots, N-1. \end{aligned} \tag{18}$$

Calculate the kurtosis values of the power spectrum and the original signal separately:

$$\begin{aligned} KPS &= \frac{m^4\{S_H(k)\}}{(m^2\{S_H(k)\})^2}, \\ Kur &= \frac{m^4\{f(n)\}}{(m^2\{f(n)\})^2}. \end{aligned} \tag{19}$$

Construct CC by combining the correlation coefficient CIC, and select the components with higher correlation with the original signal. The expression for CIC is as follows:

$$CIC = |CC| \cdot Kur \cdot KPS. \tag{20}$$

Compared with several common fault feature vectors, CIC streamlines the process of constructing analysis functions and calculating envelope spectra, thereby accelerating the calculation speed. Simultaneously, kurtosis calculations are performed on the collected signal and the signal after multiple transformations to prevent the loss of useful information during transformation. The multiplication of two kurtosis values enhances the characteristics of fault pulses, facilitating the detection of fault information in the collected signals. Considering the advantages of CC, filtering the signal by discarding components with lower correlation to the original signal proves beneficial in reducing background noise interference and emphasizing the characteristics of fault impacts.

Envelope entropy is the entropy value corresponding to the data sequence e_j obtained after envelope demodulation of the signal, which can effectively reflect the sparsity characteristics of the signal. Express the envelope entropy of signal $x(j)$ $(j = 1, 2, \ldots, N)$ as EE:

$$\begin{cases} EE = -\sum_{j=1}^{N} e_j \lg e_j, \\ e_j = \frac{a(j)}{\sum_{j=1}^{N} a(j)}, \end{cases} \tag{21}$$

where e_j is the normalized form of $a(j)$; $a(j)$ is the envelope signal of signal $x(j)$, which is decomposed by VMD and transformed by *Hilbert* from K IMF components; N is the number of sampling points.

To verify the effectiveness of the proposed feature extraction, the fifth section employs a Least Squares Support Vector Machine (LSSVM) for validation of the proposed method.

LSSVM represents an advancement over traditional SVM, featuring enhanced convergence speed and heightened recognition accuracy. Consequently, it finds widespread application in various domains, including fault recognition. The specific workflow is delineated as follows.

Assuming the training sample set $D = \{(x_i, y_i), i = 1, 2, \ldots n\}$, the objective function of LSSVM is:

$$\min_{(\omega,b,\xi)} J(\omega, \xi) = \frac{1}{2}||\omega||^2 + \frac{c}{2}\sum_{i=1}^{n}\xi_i^2. \tag{22}$$

Its constraint conditions are:

$$y_i[\omega^T\phi(x_i) + b] = 1 - \xi_i. \tag{23}$$

In the formula, ω is the weight vector; b is the bias amount; c is the penalty factor; ξ_i is the error variable.

The expression of the Lagrangian function is:

$$L(\omega, b, \xi_i, \alpha_i) = J(\omega, \alpha_i) - \sum_{i=1}^{n}\alpha_i\{y_i[\omega^T\phi(x_i) + b] - 1 + \xi_i\}, \tag{24}$$

where $L(\omega, b, \xi_i, \alpha_i)$ is the objective function for solving the optimization problem; α_i is the Lagrange multiplier.

By taking the partial derivative of parameters such as $\omega, b, \xi_i, \alpha_i$ and setting them to 0, utilizing the radial basis kernel function, we can derive:

$$\begin{cases} \frac{\partial L}{\partial \omega} = 0 \to \omega = \sum_{i=1}^{n}\alpha_i\varphi(x_i), \\ \frac{\partial L}{\partial b} = 0 \to \sum_{i=1}^{n}\alpha_i = 0, \\ \frac{\partial L}{\partial \xi_i} = 0 \to \alpha_i = \gamma\xi_i, \\ \frac{\partial L}{\partial \alpha_i} = 0 \to \omega^T\varphi(x_i) + b + \xi_i - y_i = 0. \end{cases} \tag{25}$$

By eliminating parameters ω and ξ_i, linear simultaneous equations can be obtained as follows:

$$\begin{pmatrix} 0 & y^T \\ y & ZZ^T + c^{-1}I \end{pmatrix}\begin{pmatrix} b \\ a \end{pmatrix} = \begin{pmatrix} 0 \\ y \end{pmatrix} \tag{26}$$

where $y = [y_1, y_2, \ldots y_n]^T$; $Z = [\phi(x_1), \phi(x_2), \ldots \phi(x_n)]^T$; c is the identity matrix of order $n \times 1$; the matrix I with elements equal to 1 is an $n \times n$ matrix; $\alpha = [\alpha_1, \alpha_2, \ldots \alpha_n]^T$.

The optimal classification function for the LSSVM method is:

$$f(x) = sgn\left[\sum_{i=1}^{n} \alpha_i y_i K(x, x_i) + b\right]. \tag{27}$$

4 EXPERIMENTAL VERIFICATION AND DISCUSSION

4.1 Effective Validation of VDM Parameter Optimization Method

To illustrate the efficacy of the VDM parameter optimization method proposed, this section employs the simulated signal depicted in Figure 6 as a case study. It compares the IMF component obtained through signal decomposition using the proposed method with the original signal component. The experimental results are presented in Figures 9, 10 and 11.

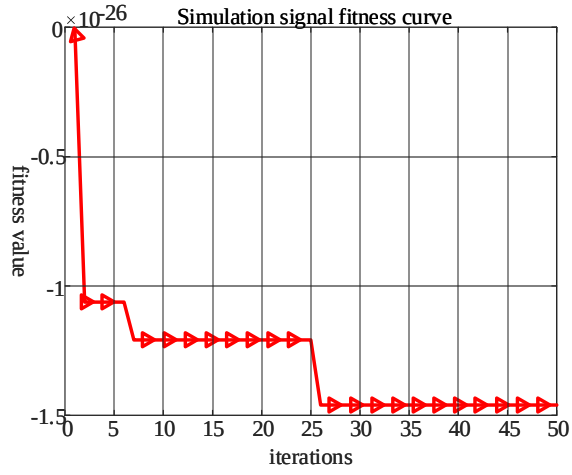

Figure 9. Simulation signal fitness curve

It is shown in Figure 9 that this method can converge on the simulated signal and reaches the optimal fitness value -1.461×10^{-26} in the 26^{th} iteration, when $K = 11$, $\alpha = 5\,456$ can be obtained.

From Figures 10 and 11, it is evident that the original component x_1 of the simulation signal corresponds to IMF1 and IMF2, the original component x_2 corresponds to IMF3, and the original component x_4 corresponds to IMF5. Each IMF component obtained through signal decomposition using this method can correspond to the original component of the simulated signal. This observation serves as

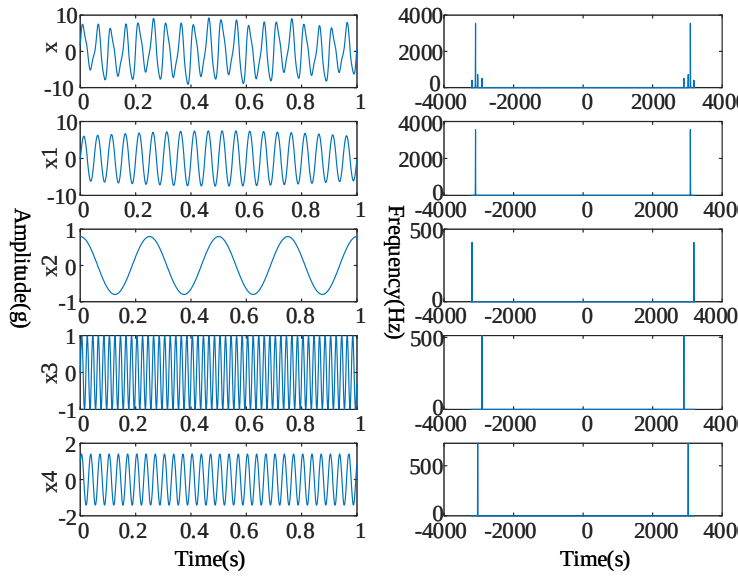

Figure 10. Time and frequency domain diagrams of simulated signals and components

empirical evidence supporting the effectiveness of employing this method for signal decomposition.

4.2 Validation of Feature Vector Validity

To validate the effectiveness of the feature vectors proposed in this study, we leverage four vibration signals sourced from the public dataset of rolling bearings at Case Western Reserve University. These signals are subjected to decomposition using the optimal parameter combination derived from the TSA-MCKD-VMD method. Subsequently, an analysis is conducted on the performance of the seven feature vectors with respect to the faults present in the corresponding MF components. To facilitate a comprehensive comparison of each feature vector's performance, the concept of normalized amplitude is introduced. This entails dividing the amplitude of each feature vector by the sum of all amplitudes. This normalization process confines the amplitude values within the range of $[0, 1]$, thereby enhancing the contrast.

Firstly, the signal of the outer ring fault is decomposed using the optimal parameter combination $K = 10$, $\alpha = 5\,004$, resulting in the generation of ten Intrinsic Mode Function (IMF) components. As illustrated in Figure 12, IMF2 and IMF3 exhibit a notable alignment with the theoretical fault frequency of 107.37 Hz and its second and third harmonics associated with the outer ring fault. Consequently,

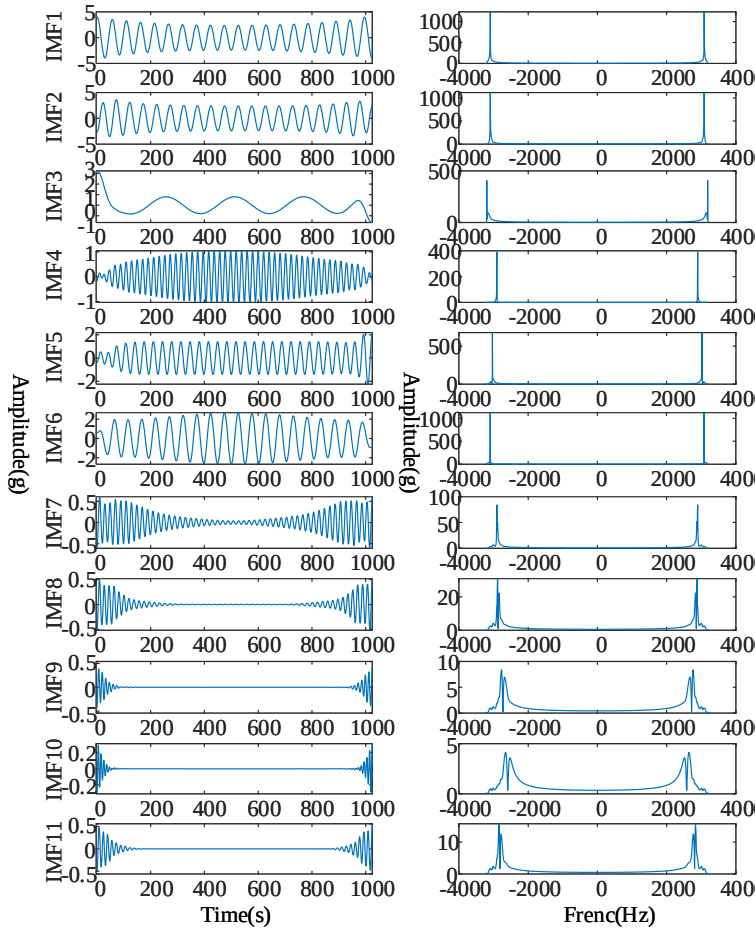

Figure 11. Time domain and frequency domain diagrams of IMF components

these IMF components can be identified as signal components harboring fault characteristic information. Figure 14 further emphasizes that IMF2 and IMF3 emerge as the most responsive components to the fault impact. Specifically, EK demonstrates heightened sensitivity to the fault impact within IMF2, while CIC exhibits the utmost sensitivity to the fault impact within IMF3.

Secondly, the signal corresponding to the inner circle fault is subjected to decomposition using the optimal parameter combination $K = 6$, $\alpha = 2893$, resulting in the generation of six IMF components. As depicted in Figure 13, IMF1 and IMF5 exhibit a close correspondence with the theoretical fault frequency of the inner ring

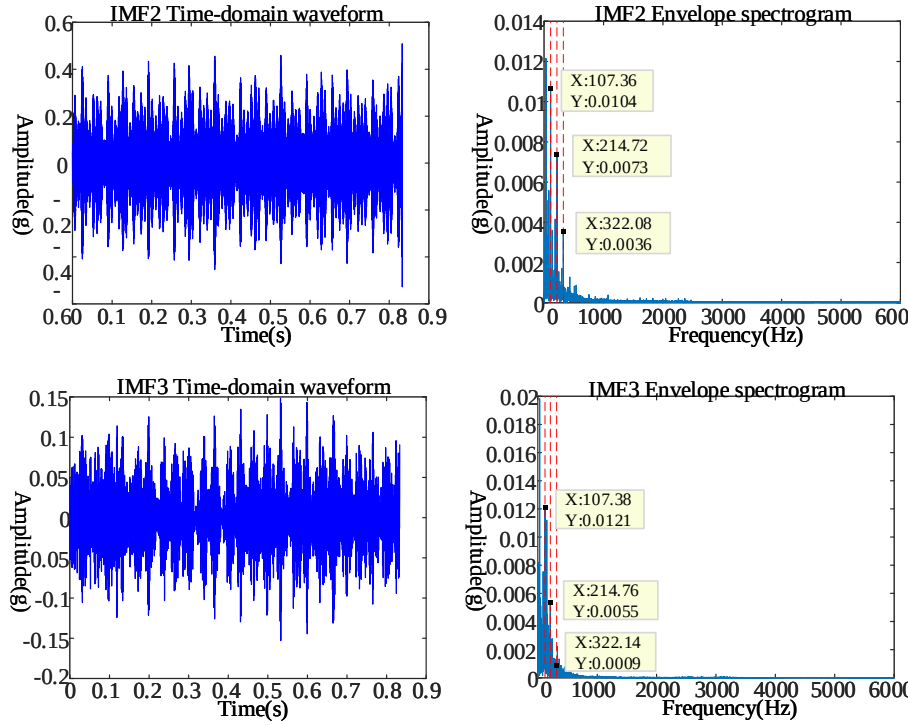

Figure 12. Decomposition results of the outer ring fault signal

fault at 162.17 Hz, along with its second and third harmonics. Consequently, these IMF components can be identified as signal components encapsulating fault characteristic information. Figure 14 further underscores that IMF1 and IMF5 emerge as the feature vectors most responsive to the impact of faults. Notably, *Kur* displays heightened sensitivity to the fault impact within IMF1, while *WK* demonstrates the utmost sensitivity to the fault impact within IMF5.

Thirdly, the signal associated with the rolling element fault undergoes decomposition using the optimal parameter combination $K = 10$, $\alpha = 4200$, resulting in the generation of ten Intrinsic Mode Function (IMF) components. As illustrated in Figure 15, IMF6 and IMF7 approximately capture the theoretical fault frequencies of rolling element faults at 70.59 Hz and its harmonics. Consequently, these IMF components can be identified as signal components containing fault characteristic information. In Figure 16, it becomes evident that IMF6 and IMF7 emerge as the feature vectors most responsive to the impact of faults. Notably, *WK* demonstrates heightened sensitivity to the fault impact within IMF6, while *KES* exhibits the utmost sensitivity to the fault impact within IMF7.

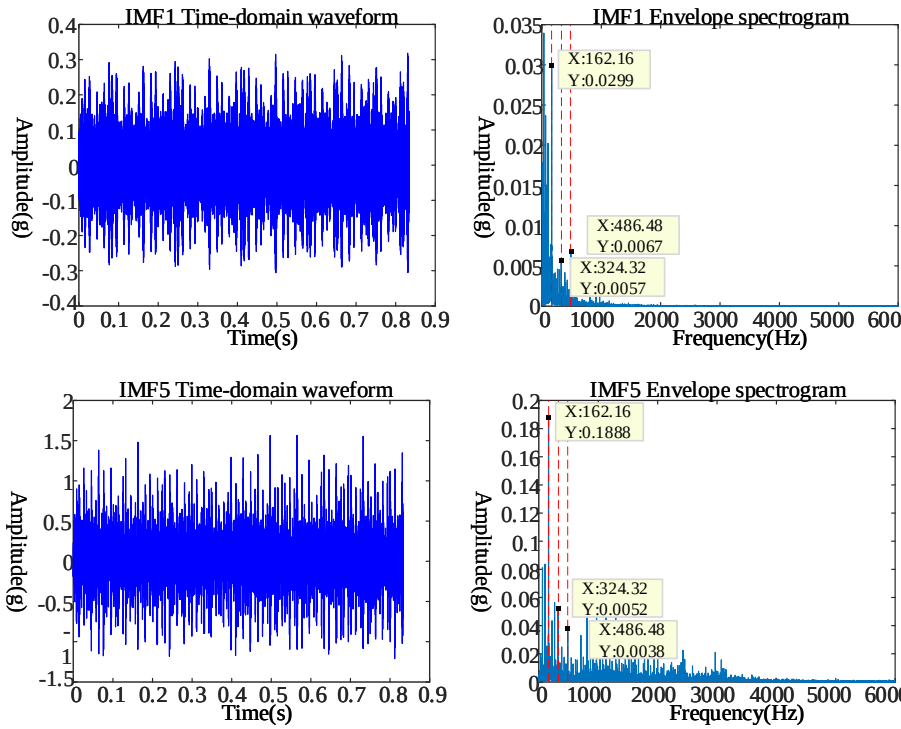

Figure 13. Decomposition results of the inner ring fault signal

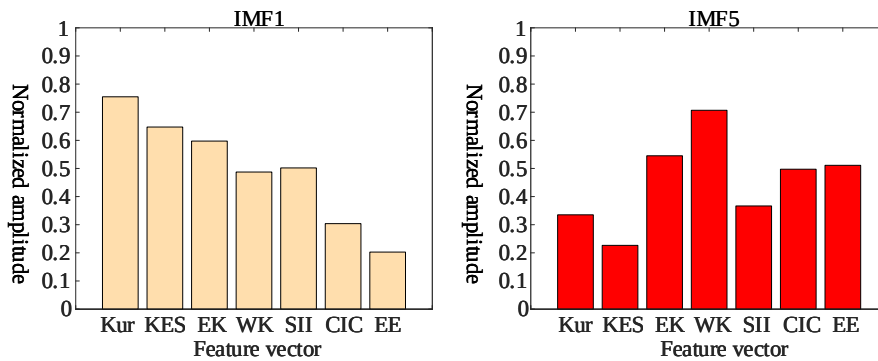

Figure 14. Comparison of characteristic parameter performance of the inner ring fault

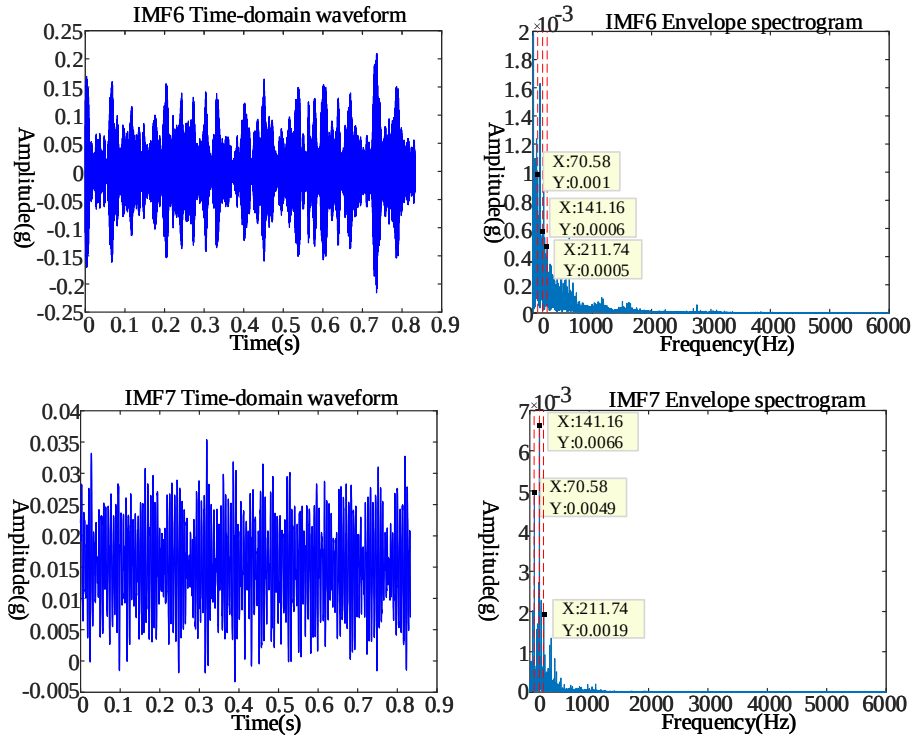

Figure 15. Decomposition results of the inner ring fault signal

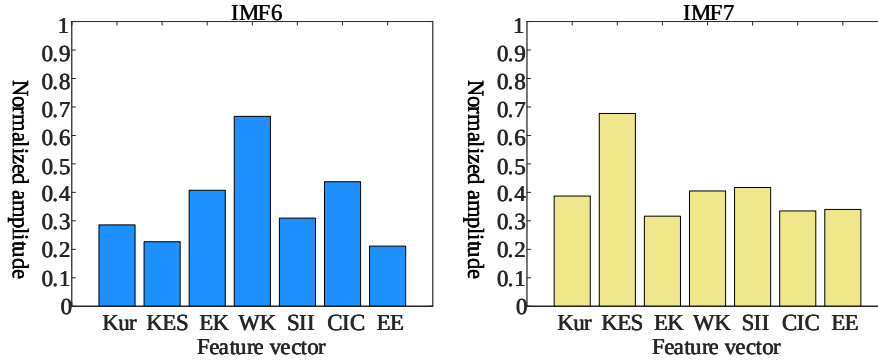

Figure 16. Comparison of characteristic parameter performance for the rolling element faults

Finally, the optimal parameter combination $K = 10$, $\alpha = 3\,900$ for the normal state signal is applied to conduct signal decomposition, resulting in the generation of ten IMF components. Analysis of Figure 17 reveals that IMF4 significantly aligns with the theoretical characteristic frequency of the normal state signal at 30 Hz, designating it as a signal component harboring fault characteristic information. Additionally, Figure 18 highlights that IMF4 stands out as the feature vector SII exhibiting the highest sensitivity to the impact of faults within the signal.

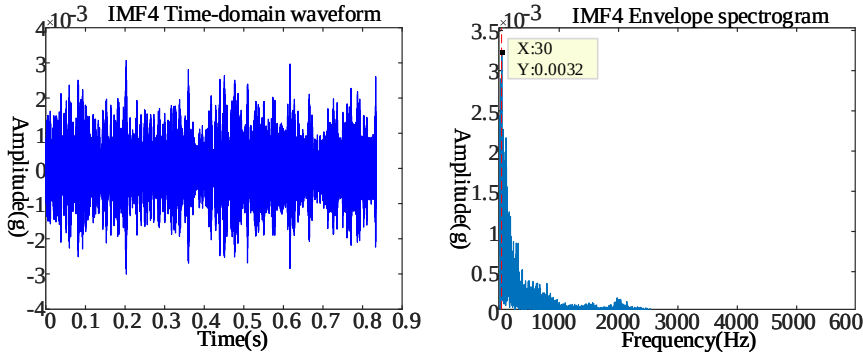

Figure 17. Decomposition results of the normal state signal

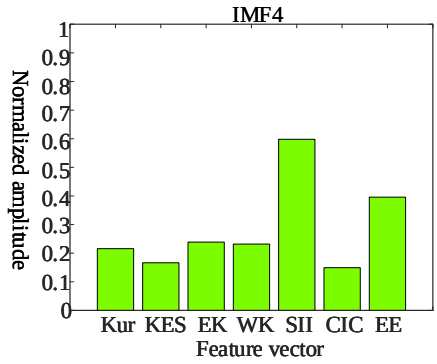

Figure 18. Comparison of characteristic parameter performance in normal state

In summary, the seven feature vectors chosen in this study exhibit distinct responsiveness to various components within different signals. Consequently, these selected feature vectors demonstrate effectiveness across all four vibration signals associated with rolling bearings.

4.3 Verification and Comparison of Feature Extraction Methods

In order to substantiate the efficacy and superiority of the proposed method for extracting fault features in rolling bearings, the LSSVM is selected as the classifier for fault types. Subsequently, a fault recognition model utilizing LSSVM is developed. Initially, a feature vector dataset was constructed, with the data length of each signal group standardized to 1024. The vibration signals from the four rolling bearings were comprehensively decomposed using the optimal parameter combination derived from the TSA-MCKD-VMD method. The feature vector dataset, encompassing multiple features, is formally represented as Equation (28):

$$\begin{pmatrix} M^1 \\ \vdots \\ M^p \end{pmatrix} = \begin{pmatrix} A_1 & B_1 & C_1 & D_1 & E_1 & F_1 & G_1 \\ \vdots & \vdots & \vdots & \vdots & \vdots & \vdots & \vdots \\ A_p & B_p & C_p & D_p & E_p & F_p & G_p \end{pmatrix}_{p\times 7}, \tag{28}$$

where p represents the total number of samples.

It is evident that the feature vector dataset is of order $(p \times 7)$. The feature vector numbers are shown in Table 4.

Serial Number	Feature Vector
A_1	Kur
B_1	KES
C_1	EK
D_1	WK
E_1	SII
F_1	CIC
G_1	EE

Table 4. The feature vector numbers

Input the constructed feature vector dataset into the LSSVM for fault recognition and determine its accuracy. Through comparative experiments involving the CS-VMD, MCKD-TSA, and CS-MCKD-VMD methods, we illustrate the effectiveness and superiority of our proposed approach.

This section conducts experiments using the extracted feature vector dataset, employing LSSVM as a classifier for fault recognition. The category labels 1, 2, 3, and 4 are assigned to denote outer ring fault, inner ring fault, rolling element fault, and normal state, respectively. Various enhancement methods, including Cuckoo Search (CS) for VMD improvement, MCKD for VMD enhancement, and the Cuckoo algorithm for VMD improvement with MCKD, are selected for comparative analysis. One hundred sets of data were randomly chosen from each of the four types of feature vector datasets, totaling 400 sets of data, with 80 % allocated for the training set and 20 % for the testing set. Ten random experiments are conducted for each of the four methods, and the average fault recognition accuracy was computed. The experimental results are presented below.

According to Table 5 and Figure 19, the test set in this experiment comprises a total of 80 samples. Among these, the CS-VMD method accurately identifies vibration signals of different categories in 76 samples, with 4 recognition errors, resulting in a fault recognition accuracy of 95 % and an average fault recognition accuracy of 93.75 %. The MCKD-VMD method demonstrates accurate identification in 77 samples, with 3 recognition errors, achieving a fault recognition accuracy of 96.25 % and an average fault recognition accuracy of 93.75 %. The CS-MCKD-VMD method accurately identifies vibration signals in 77 samples, with 3 recognition errors, leading to a fault recognition accuracy of 96.25 % and an average fault recognition accuracy of 93.875 %. In the case of the TSA-MCKD-VMD method, accurate identification is observed in 78 samples, with only 2 instances of outer ring fault samples being mistakenly identified as inner ring faults, resulting in a fault recognition accuracy of 97.5 % and an average fault recognition accuracy of 97.14 %. The superior values of average fault recognition accuracy and fault recognition accuracy in comparison to the other three methods indicate commendable fault recognition stability.

In order to further verify the effectiveness of the proposed method, an experimental platform was set up. The experimental platform is shown in Figure 20. The experimental results are shown in Table 6.

Number	TSA-MCKD-VMD	CS-VMD	MCKD-VMD	CS-MCKD-VMD
1	97.5 %	93.75 %	92.5 %	93.75 %
2	97.5 %	92.5 %	95 %	92.5 %
3	96.3 %	93.75 %	93.75 %	93.75 %
4	97.5 %	93.75 %	92.5 %	92.5 %
5	97.5 %	95 %	91.25 %	95 %
6	97.5 %	93.75 %	92.5 %	93.75 %
7	96.3 %	92.5 %	96.25 %	96.25 %
8	97.5 %	93.75 %	93.75 %	92.5 %
9	97.5 %	93.75 %	95 %	95 %
10	96.3 %	95 %	95 %	93.75 %
Average fault identification accuracy	97.14 %	93.75 %	93.75 %	93.875 %

Table 5. Results of random experiments

In summary, through the fusion of diverse feature vectors, experimental validation has demonstrated that the fault feature extraction method proposed in this paper attains the highest accuracy in fault recognition. This method exhibits robust fault recognition stability and holds notable implications for the practical implementation of rolling bearing fault feature extraction.

Number	TSA-MCKD-VMD	CS-VMD	MCKD-VMD	CS-MCKD-VMD
1	97 %	93.5 %	93 %	93.5 %
2	96.5 %	92.5 %	93.5 %	92.5 %
3	96.5 %	93.7 %	93.75 %	93.75 %
4	97.5 %	93 %	93.5 %	93.5 %
5	96.5 %	95 %	91.5 %	95.5 %
6	97.5 %	93.75 %	92.5 %	93.75 %
7	96.5 %	92.5 %	96 %	97.25 %
8	97 %	93 %	93.5 %	91.5 %
9	97.5 %	93.5 %	95.5 %	94.5 %
10	96.5 %	95 %	95 %	93.75 %
Average fault identification accuracy	97 %	93.55 %	94 %	93.95 %

Table 6. Results of bearing fault diagnosis simulation test platform

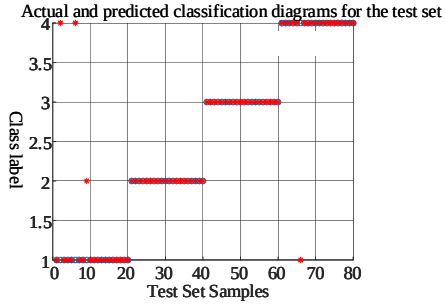

a) CS-VMD Fault recognition effect diagram of method test set

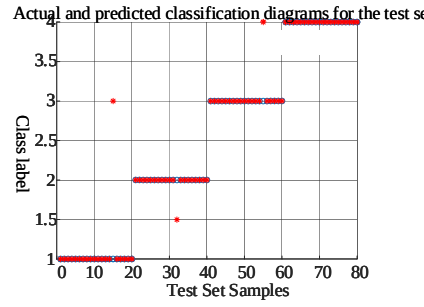

b) MCKD-VMD Fault recognition effect diagram of method test set

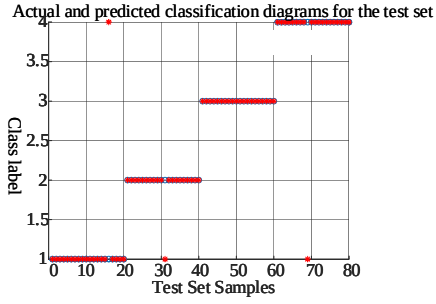

c) CS-MCKD-VMD Fault recognition effect diagram of method test set

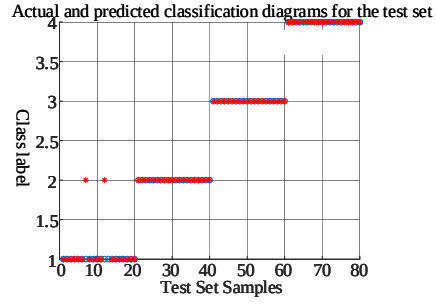

d) TSA-MCKD-VMD Fault recognition effect diagram of method test set

Figure 19. The optimal fault recognition performance of four test sets using different method

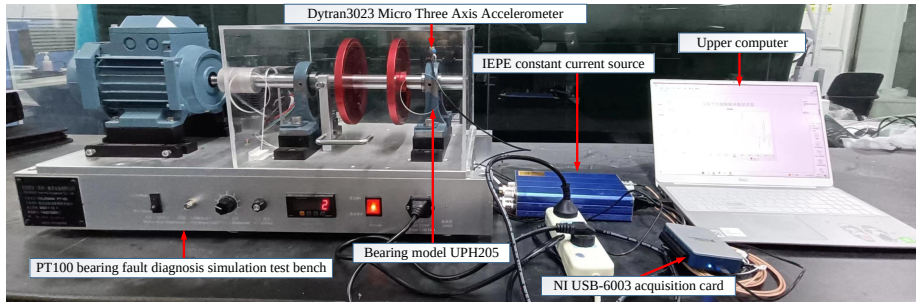

Figure 20. Bearing fault diagnosis simulation test platform

5 SUMMARY

This paper focuses on various types of vibration signals of rolling bearings, aiming to enhance the accuracy of fault recognition in this specific machinery component, and introduces a novel TSA-MCKD-VMD fault feature extraction method. Through experimentation with a standardized dataset of rolling bearings, the study shows the effectiveness of the method in extracting fault features, providing valuable insights and practical implications for the application of fault feature extraction in rolling bearings.

6 FUTURE WORK

The feature extraction method proposed in this paper can improve the accuracy of fault recognition for rolling bearings, but there are still areas that need further improvement. The fault state studied in this paper only includes one type. Considering that rolling bearings are prone to multiple types of faults in complex working conditions, further research can consider studying more types of bearing faults and extracting features of complex faults in multiple working conditions.

Acknowledgement

The authors wish to express their gratitude for the financial support from the National Natural Science Foundation of China (Grants No. 62073198, No. 62273211).

REFERENCES

[1] Hashimoto, S.—Komata, H.—Okazaki, S.—Matsunaga, H.: Quantitative Evaluation of the Flaking Strength of Rolling Bearings with Small Defects as

a Crack Problem. International Journal of Fatigue, Vol. 119, 2019, pp. 195–203, doi: 10.1016/j.ijfatigue.2018.10.003.

[2] Zhou, H.—Chen, J.—Dong, G.—Wang, H.—Yuan, H.: Bearing Fault Recognition Method Based on Neighbourhood Component Analysis and Coupled Hidden Markov Model. Mechanical Systems and Signal Processing, Vol. 66–67, 2016, pp. 568–581, doi: 10.1016/j.ymssp.2015.04.037.

[3] El-Thalji, I.—Jantunen, E.: A Descriptive Model of Wear Evolution in Rolling Bearings. Engineering Failure Analysis, Vol. 45, 2014, pp. 204–224, doi: 10.1016/j.engfailanal.2014.06.004.

[4] Yaqub, M. F.—Loparo, K. A.: An Automated Approach for Bearing Damage Detection. Journal of Vibration and Control, Vol. 22, 2016, No. 14, pp. 3253–3266, doi: 10.1177/1077546314562621.

[5] Zhao, D.—Li, J.—Cheng, W.—Wang, T.—Wen, W.: Rolling Element Bearing Instantaneous Rotational Frequency Estimation Based on EMD Soft-Thresholding Denoising and Instantaneous Fault Characteristic Frequency. Journal of Central South University, Vol. 23, 2016, No. 7, pp. 1682–1689, doi: 10.1007/s11771-016-3222-x.

[6] Guo, T.—Deng, Z.: An Improved EMD Method Based on the Multi-Objective Optimization and Its Application to Fault Feature Extraction of Rolling Bearing. Applied Acoustics, Vol. 127, 2017, pp. 46–62, doi: 10.1016/j.apacoust.2017.05.018.

[7] Zhang, X.—Zhou, J.: Multi-Fault Diagnosis for Rolling Element Bearings Based on Ensemble Empirical Mode Decomposition and Optimized Support Vector Machines. Mechanical Systems and Signal Processing, Vol. 41, 2013, No. 1–2, pp. 127–140, doi: 10.1016/j.ymssp.2013.07.006.

[8] Wang, H.—Chen, J.—Dong, G.: Feature Extraction of Rolling Bearing's Early Weak Fault Based on EEMD and Tunable Q-Factor Wavelet Transform. Mechanical Systems and Signal Processing, Vol. 48, 2014, No. 1–2, pp. 103–119, doi: 10.1016/j.ymssp.2014.04.006.

[9] Lu, Y.—Xie, R.—Liang, S. Y.: CEEMD-Assisted Bearing Degradation Assessment Using Tight Clustering. The International Journal of Advanced Manufacturing Technology, Vol. 104, 2019, No. 1, pp. 1259–1267, doi: 10.1007/s00170-019-04078-2.

[10] He, C.—Niu, P.—Yang, R.—Wang, C.—Li, Z.—Li, H.: Incipient Rolling Element Bearing Weak Fault Feature Extraction Based on Adaptive Second-Order Stochastic Resonance Incorporated by Mode Decomposition. Measurement, Vol. 145, 2019, pp. 687–701, doi: 10.1016/j.measurement.2019.05.052.

[11] Dragomiretskiy, K.—Zosso, D.: Variational Mode Decomposition. IEEE Transactions on Signal Processing, Vol. 62, 2014, No. 3, pp. 531–544, doi: 10.1109/TSP.2013.2288675.

[12] Li, T. X.—Zhang, F. D.—Lin, J.—Bai, X. Y.—Liu, H. Z.: Fading Noise Suppression Method of Φ-OTDR System Based on GA-VMD Algorithm. IEEE Sensors Journal, Vol. 23, 2023, No. 19, pp. 22608–22619, doi: 10.1109/JSEN.2023.3306199.

[13] Kumar, A.—Zhou, Y.—Xiang, J.: Optimization of VMD Using Kernel-Based Mutual Information for the Extraction of Weak Features to Detect Bearing Defects. Measurement, Vol. 168, 2021, Art. No. 108402, doi:

10.1016/j.measurement.2020.108402.

[14] Qiao, Z. K.—Yuan, P.—Zhang, J. J.—Zhang, Z. Y.—Li, L. L.—Zhu, D.—Jiang, M. R.—Shi, H. Y.—Hu, R.—Zhou, F.—Wang, Q. Y.—Zhou, Y.—Wu, B.—Lin, Q.: Error Analysis and Filtering Methods for Absolute Ocean Gravity Data. IEEE Sensors Journal, Vol. 23, 2023, No. 13, pp. 14346–14355, doi: 10.1109/JSEN.2023.3272551.

[15] Diao, X.—Jiang, J.—Shen, G.—Chi, Z.—Wang, Z.—Ni, L.—Mebarki, A.—Bian, H.—Hao, Y.: An Improved Variational Mode Decomposition Method Based on Particle Swarm Optimization for Leak Detection of Liquid Pipelines. Mechanical Systems and Signal Processing, Vol. 143, 2020, Art. No. 106787, doi: 10.1016/j.ymssp.2020.106787.

[16] Wei, W.—He, G.—Yang, J.—Li, G.—Ding, S.: Tool Wear Monitoring Based on the Gray Wolf Optimized Variational Mode Decomposition Algorithm and Hilbert–huang Transformation in Machining Stainless Steel. Machines, Vol. 11, 2023, No. 8, Art. No. 806, doi: 10.3390/machines11080806.

[17] Kaur, S.—Awasthi, L. K.—Sangal, A. L.—Dhiman, G.: Tunicate Swarm Algorithm: A New Bio-Inspired Based Metaheuristic Paradigm for Global Optimization. Engineering Applications of Artificial Intelligence, Vol. 90, 2020, Art. No. 103541, doi: 10.1016/j.engappai.2020.103541.

[18] McDonald, G. L.—Zhao, Q.—Zuo, M. J.: Maximum Correlated Kurtosis Deconvolution and Application on Gear Tooth Chip Fault Detection. Mechanical Systems and Signal Processing, Vol. 33, 2012, pp. 237–255, doi: 10.1016/j.ymssp.2012.06.010.

[19] Sun, J.—Xiao, Q.—Wen, J.—Wang, F.: Natural Gas Pipeline Small Leakage Feature Extraction and Recognition Based on LMD Envelope Spectrum Entropy and SVM. Measurement, Vol. 55, 2014, pp. 434–443, doi: 10.1016/j.measurement.2014.05.012.

[20] He, X.—Zhou, X.—Yu, W.—Hou, Y.—Mechefske, C. K.: Adaptive Variational Mode Decomposition and Its Application to Multi-Fault Detection Using Mechanical Vibration Signals. ISA Transactions, Vol. 111, 2021, pp. 360–375, doi: 10.1016/j.isatra.2020.10.060.

[21] Zhang, W.—Li, J.—Li, T.—Ge, S.—Wu, L.: Research on Feature Extraction and Separation of Mechanical Multiple Faults Based on Adaptive Variational Mode Decomposition and Comprehensive Impact Coefficient. Measurement Science and Technology, Vol. 34, 2023, No. 2, Art. No. 025110, doi: 10.1088/1361-6501/aca117.

Xuezhen Cheng received her Bachelor's degree in electrical automation from the Shandong Mining Institute, China, in 1987. She received her Master's degree in measurement technology and instrumentation from the Shandong University of Science and Technology, in 2003. She received her Ph.D. degree in control theory and control engineering from the Shandong University of Science and Technology, China, in 2011. Her research interests include power system automation, inspection technology and system integration, and information and image processing. She is currently Professor with the College of Electrical Engineering and Automation, Shandong University of Science and Technology, Qingdao, China, where she is also the Director of the Automation Department.

Chuannuo Xu is currently pursuing his Ph.D. degree in the Shandong University of Science and Technology. He received Bachelor's degree in measurement and control technology and instrument from Qilu University of Technology, Shandong, China, in 2015. He received his Master's degree in control theory and control engineering from the Shandong University of Science and Technology, China, in 2018. His research interests include detection technology and automation device, signal processing, fault diagnosis.

Hanlin Sun received his B.Eng. degree from the Changchun University of Technology, his M.Sc. degree from the Shandong University of Science and Technology, China, in 2020 and 2023, respectively. His main research interests include detection technology and automatic equipment.

Jiming Li received his B.Eng. degree, the M.Sc. degree and his Ph.D. degree from the Shandong University of Science and Technology, China, in 2009, 2012, and 2022, respectively. His main research interests include sensors and intelligent instruments. He is currently a lecturer of control science and engineering at Shandong University of Science and Technology.